Tsunami wavefront backprojection to locate sources of dispersive waves imaged by SWOT during the 2025 M8.8 Kamchatka Earthquake

Diego Melgar[1], Ángel Ruiz-Angulo[2] & Aditya Gusman[3]

[1]*Department of Earth Sciences, University of Oregon, Eugene, OR, USA*
[2] *Institute of Earth Sciences, University of Iceland, Reykjavik, Iceland*
[3] *Earth Sciences New Zealand, Lower Hutt, New Zealand*

ABSTRACT

The 29 July 2025 M8.8 Kamchatka earthquake generated a Pacific-wide tsunami that the Surface Water and Ocean Topography (SWOT) mission imaged about 70 minutes later, about 600 km from the source, as a leading crest trailed by a train of short-wavelength dispersive waves. Rather than matching an assumed source forward to the observations, as prior studies of this wavefield have done, we back-project the observed wavefronts. Using a dispersive ray-tracing engine and travel-time reciprocity, we trace each digitized, band-passed front to a source location and, from SWOT's per-pixel acquisition times to an emission time, with no assumed source model parameters. The method recovers the known source region from the leading front, and per-front resolution is quantified by a bootstrap calibrated against blind re-digitization. Because a single front constrains an arc of source positions traded against emission time, many fronts are not localizable and are left uninterpreted. Ten trailing fronts are nonetheless robustly localized outside the coseismic source region and at emission times well after the origin. Their emission time increases with distance from the source, and each was emitted later than the earliest possible arrival of energy from the earthquake at its location. Independently of the back-projection, the whole trailing train is shown to arrive too late to have been radiated dispersively from the source. A substantial part of the short-wavelength tail imaged by SWOT therefore did not originate at the coseismic source but was generated along the propagation path, progressively delayed through interaction with the seafloor. Back-projection of wide-swath altimetry locates and times the origin of individual tsunami waves directly from the observed wavefield.

Key Points:

1. We back-project the dispersive tsunami wavefield SWOT imaged after the 2025 Kamchatka earthquake to locate and time individual wavefronts, with no assumed source model.
2. Ten trailing short-wavelength fronts are robustly located outside the coseismic source region and emitted well after the origin time.
3. Their emission times and the late arrival of the whole train indicate short-wavelength energy generated during propagation, not radiated from the source.

Plain Language Summary

When a large undersea earthquake makes a tsunami, most of the wave energy comes from the seafloor that moved during the quake. But tsunamis can also pick up shorter, more complex waves as they travel across a rough seafloor, and telling the two apart is difficult. In July 2025 a major earthquake off Kamchatka sent a tsunami across the Pacific, and by chance the SWOT satellite, which maps the sea surface in two dimensions rather than along a single line, passed overhead about 70 minutes later and photographed the wavefield, including a train of short waves trailing the main front. We developed a way to run these waves backward in time over the real ocean depth to find where and when each one started, without assuming anything about the earthquake. Most of the short waves we could trace did not come from the earthquake itself. They started far from it and well after it, and later the farther out they began, which shows they were created as the tsunami traveled, by its interaction with the seafloor along the way. The approach works on any tsunami that a wide-view satellite like SWOT happens to catch, and could help locate the source of future events.

1. Introduction and Motivation

The tsunami hazard posed by great subduction-zone earthquakes is governed by the specific details of how coseismic slip is distributed over the causative fault. Slip concentrated near the trench displaces the seafloor with larger amplitude, over short horizontal length scales, and with steep gradients, producing disproportionately large, short-wavelength sea-surface perturbations that dominate near-field runup (e.g. Satake, 1994; Hill et al., 2012; Melgar et al., 2016). In contrast, slip concentrated down-dip generates broader, long-wavelength uplift and a comparatively modest tsunami (e.g., Tanioka et al., 2004; Gusman et al., 2015; Ye et al., 2022). The 2025 M8.8 Kamchatka earthquake (Figure 1) and its 1952 M9.0 predecessor on the same margin illustrate the point directly: despite comparable along-strike extent, the down-dip 2025 rupture produced a far less destructive tsunami than the 1952 event (MacInnes et al., 2010; Ruiz-Angulo et al., 2025; Pinegina et al., 2025). A recent re-examination of the 1952 earthquake shows that large slip locates near the trench, but and that the largest slip region is located at ~30 km, depth-wise comparable to the 2025 event (Gusman 2026) Because the shallowest portion of the rupture is at once the most tsunamigenic and the most consequential for hazard, resolving whether and where a great earthquake breaks the near-trench region is a first-order problem in tsunami science.

It is also among the hardest to constrain. The near-trench plate interface is poorly imaged by teleseismic and geodetic data: it is far offshore, beyond the reach of onshore GNSS and InSAR, and its shallow dip and low rigidity make it seismically inefficient, so finite-fault and rapid-slip inversions carry their largest uncertainties precisely where the tsunami is most sensitive to slip (e.g. Romano et al. 2012; Satake et al., 2013; Yue et al., 2014). Deep-ocean pressure sensors (DART) partially fill this gap but sample the wavefield at only a handful of points, and their bottom-pressure response can somewhat attenuate the short-wavelength components that carry near-trench information. Meanwhile, conventional nadir satellite altimetry has occasionally captured tsunami fronts, but its along-track geometry yields one-dimensional sea-surface profiles that cannot resolve wavelength, wavefront curvature, or propagation direction (Okal et al., 1999; Kulikov, 2006; Hayashi, 2008; Song et al., 2012). The observational quantities most diagnostic of a near-trench source are therefore the ones legacy instruments are least able to measure.

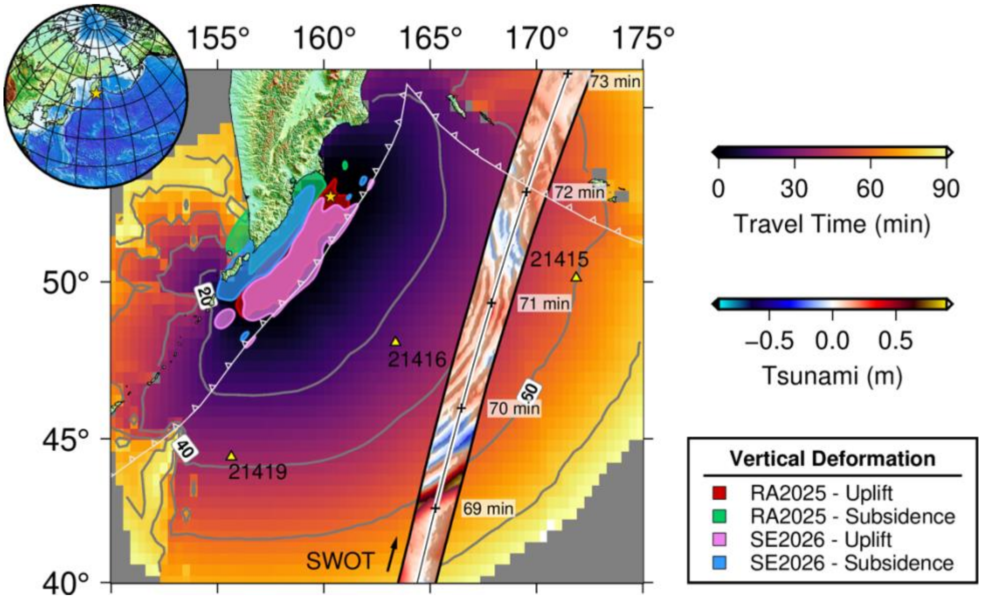

Figure 1. *Regional setting of the 29 July 2025 M8.8 Kamchatka earthquake and the SWOT observation of the resulting tsunami. The yellow star marks the USGS epicenter. The background color field shows modeled tsunami travel time (minutes), where each pixel gives the minimum travel time to that point over a set of point sources distributed at 20 km spacing within the near-trench source region of Sepúlveda et al. [2026]. The SWOT swath from ascending pass 267 is outlined in black, with the near-nadir gap shown, and the background-removed sea-surface height anomaly measured along it is shown in the blue-white-red color scale). Black crosses along the swath and the accompanying labels (69–73 min) give the time after origin at which SWOT imaged each along-track position. Shaded patches near the coast show the preferred initial sea-surface disturbance of the two prior source studies, each bounded by its +0.2 m and −0.2 m contours: red and green for the positive and negative disturbance of Ruiz-Angulo et al. [2025] (RA2025), pink and blue for those of Sepúlveda et al. [2026] (SE2026). Yellow triangles mark the DART bottom-pressure sensors) referenced in the text.*

The Surface Water and Ocean Topography (SWOT) mission changes this. Its Ka-band radar interferometer measures sea-surface height along a wide (~120 km) swath at centimeter precision, resolving two-dimensional features at ~10–100 km scales (Morrow et al., 2019; Vinogradova, 2025). For the first time, a single overpass images not just the amplitude of a very large tsunami but the geometry of its wavefield, wavelength content, front curvature, and propagation direction, over hundreds of kilometers. Roughly 70 minutes after the 29 July 2025 Kamchatka earthquake (M8.8; 23:24 UTC), SWOT ascending pass 267 intersected the expanding wavefield ~600 km seaward of the source (Figure 1) and recorded a leading long-wavelength crest trailed by a train of at least seven shorter-wavelength waves (Ruiz-Angulo et al., 2025; Sepúlveda et al., 2026). This dataset is, to our knowledge, the most detailed two-dimensional image ever obtained of a great tsunami's near- to intermediate-source wavefield, and it has already motivated two independent source studies.

That a train of dispersive, short-wavelength waves appears at all is itself notable. Frequency dispersion scales with the square of the depth-to-wavelength ratio, so a rupture several hundred kilometers in extent, radiating predominantly long waves, would be expected to propagate in the near-shallow-water limit with little dispersion (Kajiura, 1963; Glimsdal et al., 2013). The presence of a coherent short-wavelength tail therefore requires that energy be present at wavelengths comparable to a few factors of the ocean depth, whether placed there by the source or produced afterward, and the question of which is discussed in two studies to have examined this wavefield. These two studies weigh the possibilities differently. Sepúlveda et al. (2026) interpret the trailing short-wavelength train (characteristic wavelength ~50 km, $\lambda/h \approx 9$, in the weakly dispersive regime) primarily as a signature of near-trench slip: shallow coseismic deformation injects short-wavelength energy into the initial sea surface, and frequency dispersion sorts it during transit so that shorter components lag behind the leading crest, a source-dispersion mechanism established for the 2009 Samoa and 2011 Tohoku tsunamis (Saito et al., 2010, 2011, 2014; Zhou et al., 2012; Kirby et al., 2013; Okal & Synolakis, 2016). From a joint DART–InSAR–SWOT slip inversion propagated with a Boussinesq model, together with off-trench and checkerboard tests, they infer tsunamigenic slip within ~10 km of the trench and an along-strike centroid between 49.5° and 52.5°N. Ruiz-Angulo et al. (2025), inverting the DART records for the initial sea-surface displacement, find a ~400 km rupture with peak uplift near 51°N concentrated further down-dip, and infer only modest, if any, near-trench slip, favoring a partial re-rupture of the deeper 1952 asperity (MacInnes et al., 2010). They note that a dispersive forward model initialized with their source under-predicts the observed trailing train and suggest that some of the short-wavelength structure is generated during propagation by interaction with the trench, continental slope, and complex bathymetry. The two accounts thus place the emphasis differently, on short-wavelength energy imparted at the source versus energy developed en-route, though both acknowledge a role for propagation over rough bathymetry, and neither excludes the other. Between these end members lies a broader set of processes that could imprint short wavelengths on a propagating tsunami and that have received little attention in this context: scattering and refraction by abyssal-hill fabric, seamounts, and fracture zones along the deep-water path; resonance and edge waves on the continental shelf; and partial trapping and re-radiation at bathymetric features. Distinguishing these requires a way to locate and time the origin of individual waves in the observed train, rather than matching the aggregate wavefield to an assumed source.

This disagreement denotes a difference in preferred models and reflects a methodological limitation shared by both previous studies. Each proceeds in the forward/inverse direction; they assume a source distribution, prescribe a propagation operator, and adjust the source until the modeled swath matches the observation. This is powerful for testing a hypothesized source, but it cannot, by construction, separate waves radiated by the source from waves generated en-route, because both are folded into a single forward simulation whose fit is then read as support for the source. Nor can it localize an individual observed wavefront without first committing to a source model and a dispersion relation. The resulting inferences inherit the non-uniqueness of the assumed source parameterization and the regularization applied to stabilize it. What is missing is a way to ask, of each observed wavefront on its own terms and without presupposing a source, where and when it originated.

Here we attempt to take that complementary approach: rather than propagating a hypothesized source forward to the swath, we back-project features of the observed wavefield from the swath toward its origin. Back-projection has become a standard tool for imaging the *seismic* rupture of great earthquakes, including this one (Kiser & Ishii, 2017; Shibata et al., 2025), but the analogous treatment of the *tsunami* wavefield that SWOT resolves has not, to our knowledge, been carried out. Backward ray tracing of tsunami travel times from receivers toward a source has been applied to refine far-field dispersion predictions (Tappin et al., 2014; Poupardin et al., 2018), a precedent for backward timing that we extend here to the source-free localization of individual two-dimensional wavefronts. Our method exploits travel-time reciprocity: for each point on a digitized wavefront we trace rays outward across the true bathymetry and read the travel time at every candidate source location, so that stacking over the front yields, for each candidate, a measure of how well it explains the observed wavefront as an isochron. The procedure requires no assumed slip distribution and no forward tsunami simulation; each traced front becomes an independent, source-model-free constraint on its own point of origin. A single far-field wavefront constrains an arc-shaped locus rather than a point, and we present that arc as the primary, assumption-light result, collapsing it to a location only when the additional timing information warrants.

That additional information is available because SWOT images each pixel at a slightly different time along its polar orbit. Every point on a traced wavefront therefore carries an absolute observation time referenced to the earthquake origin, and the back-projection returns not only where a front originated but, through a simple grid search, when it was most likely emitted. This converts a purely geometric arc constraint into a joint constraint on source location and emission time, a quantity neither prior study used for localization, and the key to distinguishing a wave radiated from at the coseismic source from one generated later, far from the epicenter, during propagation. The same machinery provides an independent test of dispersion itself: when we back-project each wavelength band using the non-dispersive shallow-water phase speed, the fronts fail to localize coherently; when we use the appropriate dispersive phase speed for the band, coherent origins are recovered. This is a geometric, localization-based confirmation of dispersion that is independent of, and complementary to, the waveform-matching arguments of the two prior studies.

Applying this framework to the narrow-band wavefronts traced across the SWOT swath, we localize a subset of the trailing fronts and recover, for each, an emission time. Back-projection of the leading front recovers the known source region, validating the method against an independent constraint. Where the picking geometry permits, ten trailing fronts are robustly localized to have originated outside the coseismic source region and at emission times well after the epicentral time, and this result is stable across the choices made in the analysis. Two properties characterize them: their emission time increases with distance from the source, and in every case they were emitted later than the earliest possible arrival of energy from the earthquake at their recovered location, by an amount that grows with distance. A direct check confirms the implication, that the entire trailing train arrives too late to have been radiated dispersively from the coseismic source. This favors, for the resolved fronts, generation during propagation, progressively delayed through interaction with the seafloor along the corridor the waves crossed, rather than radiation of short-wavelength energy from the source itself. The many fronts that the geometry cannot localize uniquely are reported as such and carry no interpretation. Back-projection thus provides what forward modeling of the aggregate wavefield cannot, a location and an emission time for individual waves, and with them a direct, source-model-free test of where the short-wavelength tail imaged by SWOT originated.

2. Data and Methods

2.1 Observations from SWOT

The Surface Water and Ocean Topography (SWOT) mission, launched in December 2022, carries the Ka-band Radar Interferometer (KaRIn), which measures sea-surface height (SSH) across two roughly 50 km sub-swaths separated by a nadir gap, giving a total swath width near 120 km. Unlike conventional nadir altimeters, which return a single one-dimensional SSH profile beneath the satellite track, KaRIn produces a two-dimensional image of the sea surface at centimeter-level precision and resolves features at horizontal scales of roughly 10 to 100 km (Morrow et al., 2019; Vinogradova, 2025). For solid-Earth and tsunami applications this is a qualitative change in what can be observed: a single overpass records the full planform of a passing wavefield, including its wavelength content, wavefront curvature, and propagation direction, rather than a lone cross-section. We refer the reader to the mission references above for instrument and orbit details and focus here on the processing that turns the SWOT image into the banded wavefronts used for back-projection.

We use the SSH anomaly from ascending pass 267 over the northwest Pacific, acquired between roughly 69 and 73 minutes after the 29 July 2025 origin time. The large-scale oceanographic background (mesoscale eddies, internal tides, and the steric and circulation signals SWOT is nominally designed to observe) has been removed following subtraction of wavelengths longer than 100 km estimated from adjacent-day gridded products, as in Ruiz-Angulo et al., (2025) and Sepúlveda et al., (2026), leaving the tsunami sea-surface height anomaly (SSHA) shown in Figures 1 and 2a. The leading front reaches SSHA amplitudes of order 0.9 m near 43°N, trailed to the north by a train of visibly shorter-wavelength, lower-amplitude waves.

2.2 Projection to a track-aligned frame and wavenumber spectra

The SWOT swath is a long, narrow strip that crosses, for this tsunami, more than fifteen degrees of latitude while remaining about 120 km wide, so neither a plate-carrée grid nor a standard map projection is well suited to spectral analysis: wavelength measured in degrees is distorted along the strip, and the along-track and cross-track directions are not grid-aligned. We therefore project the SSHA into a Hotine Oblique Mercator frame (Figure 2a) whose central line follows the ground track (central point 167.8°E, 49.2°N; track azimuth 16.5°), so that one Cartesian axis runs roughly along-track and the other cross-track. The projection is conformal, so it preserves local angles and, to a very good approximation over a strip this narrow, preserves wavelength, which is the property we need for spectral estimation. Within this frame the SSHA is resampled onto a regular 1 km grid.

To characterize the wavelength content of the wavefield and its evolution along the swath, we extract a set of one-dimensional profiles that cross the wave train perpendicularly at successive along-track positions, progressing from the leading front in the south to the trailing waves in the north (profiles 0 to 4 in Figure 2a,b). The five profile lines were are positioned approximately perpendicular to the tsunami wavefronts crossing multiple wave crests and troughs. Along each profile we sample the gridded SSHA at 1 km spacing, discard the swath-edge buffer, linearly detrend to remove any residual large-scale slope, and estimate the wavenumber spectrum with Thomson's multitaper method (time-bandwidth product NW = 4 and eight tapers), which gives a low-variance spectral estimate well suited to short records (Thomson, 1982; Prieto et al., 2022). The resulting spectra (Figure 2b) show a clear progression: the leading front is dominated by wavelengths near and above 60 km, while the trailing profiles carry progressively more power at shorter wavelengths, developing distinct spectral peaks below 60 km. This behavior is the wavenumber-domain expression of dispersion, with the longer components leading and the shorter components trailing. We use a wavelength of 60 km as a practical divider between the long leading arrival and the shorter, dispersed trailing waves (dashed line in Figure 2b); note that this is a descriptive boundary chosen from the spectra, not a physical cutoff.

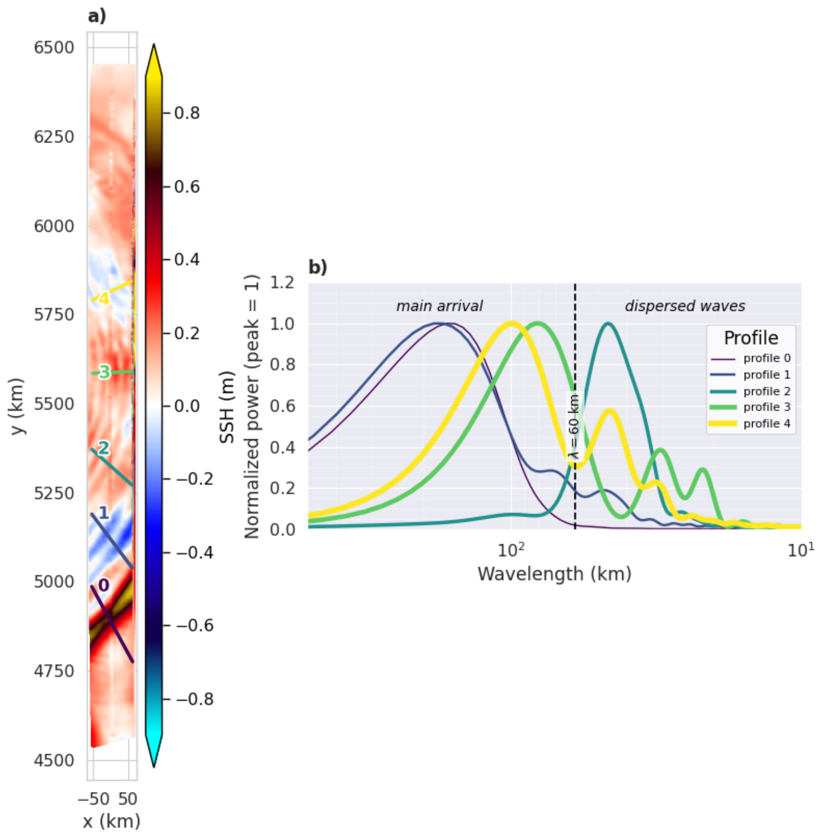

Figure 2. *Wavenumber content of the SWOT wavefield along the swath. (a) Tsunami SSH anomaly from pass 267 projected into the track-aligned Hotine Oblique Mercator frame. The five lines are the profiles along which spectra are computed, numbered 0 to 4 and colored from south to north, progressing from the leading front into the trailing wave train. (b) Multitaper wavenumber spectra of the profiles in (a), plotted against wavelength each normalized to unit peak power; line color matches the profiles in (a) and line width increases northward. The dashed line at 60 km marks the descriptive boundary used to separate the long leading arrival from the shorter dispersed waves.*

2.3 Band-pass decomposition of the wavefield

Guided by the spectra, we separate the wavefield into a set of wavelength bands so that individual wavefronts can be isolated and traced. Working in the same track-aligned frame from Figure 2a, we remove a static offset estimated over a quiet along-track window, take the two-dimensional Fourier transform of the gridded SSHA on a zero-padded grid, and apply a radial Butterworth filter (order 8) in wavenumber magnitude before transforming back to physical space. We compute one long-wavelength band spanning 80 to 300 km (Figure 3a), which captures the leading long-wave arrival at

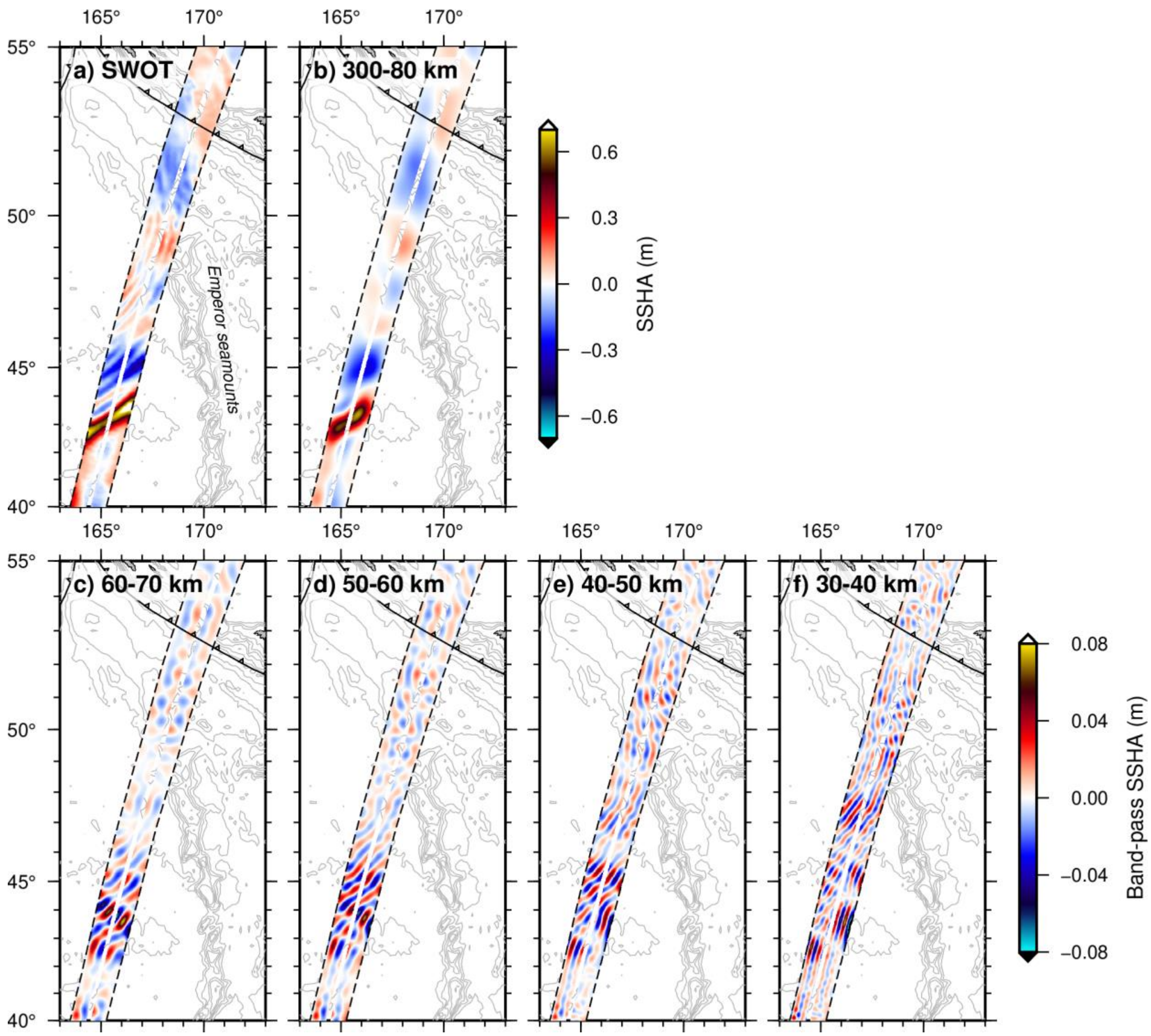

Figure 3. *SWOT sea-surface height anomaly across the July 2025 Kamchatka tsunami. (a) The filtered SSHA and (b) its 300–80 km band, sharing the SSHA color scale. (c–f) Band-passed SSHA at 60–70, 50–60, 40–50, and 30–40 km, sharing the band-pass color scale, which is roughly an order of magnitude finer because the dispersed waves reach only a few centimeters against the half-meter leading crest. Dashed lines mark the swath edges and nadir gap; the trench is shown throughout and the Emperor Seamounts are labelled in (a).*

close to full amplitude, and four narrower bands at 60 to 70, 50 to 60, 40 to 50, and 30 to 40 km that isolate successive portions of the dispersed tail (Figures 3b to 3f). Each filtered band is then inverse-projected from the track-aligned frame back to geographic coordinates for wavefront tracing and back-projection (Section 3).

The decomposition makes the trailing wave train tractable. In the full SSHA (Figure 3a) the low-amplitude dispersed waves are overwhelmed by the leading crest, but once separated by wavelength they appear as coherent, quasi-periodic sets of crests and troughs with amplitudes of a few centimeters, roughly an order of magnitude below the leading front (note the change of color scale between Figure 3a,b and Figures 3c to 3f). The shorter-wavelength bands show wave packets that are increasingly numerous and increasingly curved, and whose crests can be followed across much of the swath width. These banded crests are the digitized wavefronts that the back-projection takes as input.

The radial filter treats wavenumber magnitude isotropically rather than filtering a single direction. This is appropriate here because the tsunami crests are locally quasi-planar, so that the along-crest wavenumber is small and the radial magnitude is dominated by the cross-crest component, which is the wavelength the spectra measure. Residual sensitivity to obliquely propagating energy, together with the mild ringing inherent to a high-order Butterworth response and edge effects near the swath boundary and the nadir gap, is considered in the tracing step, where only crests that are coherent across the swath are retained.

2.4 Ray-tracing framework: From the shallow water approximation to dispersion

To solve the back-projection problem we built a tsunami ray-tracing code, TsunamiTrace, that propagates wavefronts as rays on a spherical Earth following the ray-theoretical treatment of Gusman et al. (2017). The ocean is represented by a regular bathymetric grid, from which we construct a slowness field

$$n = \frac{1}{c} \; , \qquad (1)$$

where c is the local tsunami wave speed. In a non-dispersive ocean a single slowness field describes everything, because every wavelength travels at the same speed. A dispersive ocean is different: the ray path bends according to one speed while wave energy travels at another. In the shallow-water, or long-wave, limit the speed is set by depth alone,

$$c_{sw} = \sqrt{gh} \; , \qquad (2)$$

with g the gravitational acceleration and h the water depth. Every wavelength then travels at the same speed and the ocean is non-dispersive. This is the standard approximation for great earthquakes, whose rupture dimensions of tens to hundreds of kilometers greatly exceed the ocean depth, so that the dominant tsunami wavelengths satisfy $kh \ll 1$, with $k = 2\pi/\lambda$ the wavenumber and λ the wavelength.

The approximation fails once the wavelength becomes comparable to the depth, which is the regime of the trailing waves imaged by SWOT. When kh is no longer small the waves feel the finite depth: shorter wavelengths travel more slowly than longer ones, and an initially compact disturbance disperses into an extended wavetrain with long waves running ahead and short waves trailing behind. The speed then follows from the full linear (Airy) dispersion relation,

$$\omega^2 = gk\tanh(kh_{ref}) \quad , \qquad (3)$$

which relates the angular frequency ω to the wavenumber k at reference depth depth h_{ref}. Two properties make this tractable for ray tracing. First, ω is conserved as a wave crosses slowly varying bathymetry whereas k is not, so a prescribed ω fixes a unique k, and hence a unique speed, at every depth. Second, the quantity a ray transports is wave energy, which travels at the group speed rather than the phase speed. The speed that enters the slowness field is therefore the dispersive group speed,

$$c_d = \frac{\omega}{2k}\left(1 + \frac{2kh}{\sinh(2kh)}\right), \tag{4}$$

evaluated with the depth-dependent k that solves the dispersion relation. This expression reproduces both limits automatically, as $kh \to 0$ it returns the shallow-water speed, recovering the non-dispersive model as a special case, and as $kh \to \infty$ it tends to the deep-water group speed $\frac{1}{2}\sqrt{(g/k)}$. Figure 4 shows how far the dispersive group speed departs from the shallow-water value across the wavelengths and depths of interest: at the abyssal depths the SWOT swath crosses, waves in the observed 30–70 km band travel well below $\sqrt{(gh)}$, and treating them with the shallow-water speed would overestimate their propagation speed, and underestimate their travel time, by an amount that grows with depth and with decreasing wavelength.

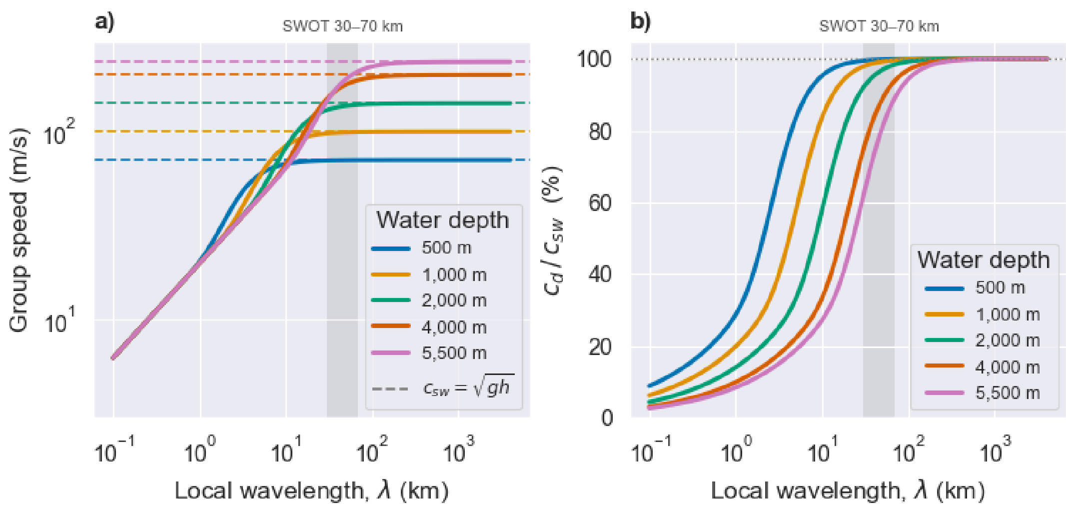

Figure 4. *Dispersion of surface gravity waves across the SWOT wavelength band, from the linear relation $\omega^2 = gk \cdot \tanh(kh)$. Plotted speed is the group speed c_d, which governs energy transport and hence travel time. (a) c_d versus local wavelength λ for five ocean depths; dashed lines mark the shallow-water limit $c_{sw} = \sqrt{(gh)}$, approached only at long wavelengths. (b) The ratio c_d/c_{sw}. The shaded band spans the 30–70 km wavelengths SWOT resolves in the trailing train; within it c_d falls well below $\sqrt{(gh)}$, and the shortfall grows with depth, reaching about 62% of c_{sw} at 30 km in 5,500 m of water.*

Each ray is a characteristic of the Eikonal equation. Writing its state as colatitude θ, longitude ϕ, and local ray direction ψ, the trajectory is governed by the coupled system

$$\frac{d\theta}{dt} = \frac{\cos(\psi)}{nR}, \tag{5}$$

$$\frac{d\varphi}{dt} = \frac{\sin(\psi)}{nR\sin(\theta)}\ , \tag{6}$$

$$\frac{d\psi}{dt} = -\frac{c_g}{c_p}\frac{sin(\psi)}{n_p^2 R}\frac{\partial n_p}{\partial \theta} + \frac{c_g}{c_p}\frac{cos(\psi)}{n_p^2 R sin(\theta)}\frac{\partial n_p}{\partial \varphi} - \frac{sin(\psi)cot(\theta)}{n_g R} \quad , \qquad (7)$$

where *R* is the Earth's radius. Equations (5) and (6) advance the ray position at the group speed c_g, with which wave energy and therefore travel time propagate, and are identical to those of Gusman et al. (2017). Equation (7) differs from that work in an essential way. Its first two terms are the spherical form of Snell's law, but because the ray is a characteristic of the Eikonal equation written in the phase slowness, the refraction is driven by the gradients of the phase slowness $n_p = 1/c_p$ rather than the group slowness, each term weighted by the factor c_g/c_p that follows from the Hamiltonian ray equations in a dispersive medium. The final term is a geometric correction for meridian convergence and correctly retains the group slowness. In the shallow-water limit $c_g = c_p$, the weighting factor becomes unity, and the system reduces to the single-slowness form of Gusman et al. (2017).

Dispersion thus enters in two distinct places: the group-speed field sets the rate at which rays advance, and hence all travel times, while the phase-speed field sets how they refract. The distinction is consequential and can have significant effects (Figure 5). Bending the rays on the group

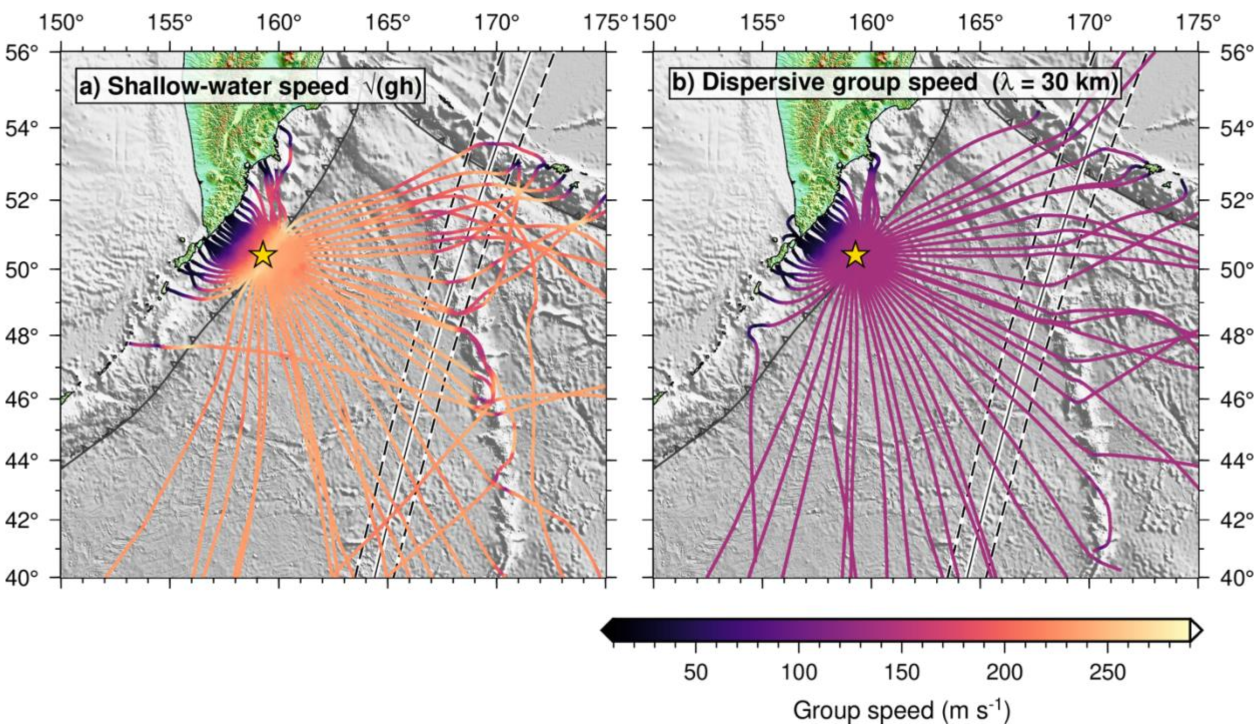

***Figure 5**. Effect of frequency dispersion on tsunami propagation for a point source (gold star) near the 2025 Kamchatka centroid (159.27°E, 50.41°N). Rays are shot at a uniform azimuth spacing and colored by the local wave speed. (a) Non-dispersive shallow-water rays, speed √(gh). (b) Rays for a wave of 30 km local wavelength at the source depth (period ≈ 2.5 min), from which the conserved frequency follows, colored by the local dispersive group speed from $\omega^2 = gk{\cdot}tanh(kh)$. Both panels share one color scale. The dispersive rays are slower, by about 40% over the abyssal plain, and they also refract differently: because bending follows the phase-slowness gradients, the two fans are not simply rescaled versions of each other, most visibly where rays cross the trench and Emperor seamounts. Dashed lines and central track mark the SWOT swath and nadir; the barbed line is the Kuril–Kamchatka trench.*

slowness instead, as a single-field implementation does, leaves the long leading wave essentially unaffected, but at λ = 30 km in 5,500 m of water it reduces the refraction to roughly 8% of its correct value, and beyond the maximum of c_g at fixed ω, which for that wave lies at a depth of 5,834 m, it reverses the sign of the bending altogether.

Because the dispersion relation is implicit in k, the wavenumber is found numerically. At every grid cell we solve

$$F(k) = \omega^2 - gk\tanh(kh) = 0 \quad (8)$$

by Newton–Raphson iteration, with derivative

$$F'(k) = -g[\tanh(kh) + kh\mathrm{sech}^2(kh)] \quad (9)$$

Starting from the shallow-water estimate $k_0 = \omega/\sqrt{(gh)}$, which lies to one side of the root because F is monotonically decreasing in k, the iteration converges one-sidedly; fifteen iterations drive the residual below machine precision across the full range of physically realistic kh, with clamping to keep k positive and overflow guards on the hyperbolic functions at large kh. Once ω is fixed the group- and phase-speed fields are static functions of depth and are computed once.

The ray system is then integrated with a vectorised fourth-order Runge–Kutta scheme at a fixed time step. The local medium, comprising the two slowness fields, their ratio, and the two gradients of the phase slowness, is evaluated once per step at the grid cell containing the ray and held fixed across the four stages. All rays, across every source and azimuth, are advanced simultaneously as array operations, and a ray is retired when it exits the grid, enters water shallower than 10 m, or reaches a dry cell. Because each ray position carries its elapsed integration time, which is the group travel time, the ray set is gridded onto a regular map that retains the earliest, first-arrival, time in each cell, yielding travel-time maps that can be sampled at arbitrary receiver locations such as SWOT pixels.

The rays are labeled according to what wave they represent through its frequency, in any equivalent form. Our observations fix that frequency through wavelength, and a spatial band-pass of a sea-surface image (Section 2.3) isolates the wavelength a wave possesses in the water it is crossing, the in-situ wavelength λ. The corresponding ω follows from the dispersion relation, Equation (3), with $k = 2\pi/\lambda$ evaluated at a reference depth h_{ref} This in-situ wavelength must be distinguished from the deep-water wavelength λ_0 that the same wave would have in infinitely deep water; the two are related by

$$\lambda_0 = \frac{\lambda}{\tanh(kh_{ref})} \quad (10)$$

and can differ substantially at the depths the SWOT swath spans. Crests 30 km apart in 5,500 m of water correspond to λ_0 = 36.7 km, and crests 70 km apart to λ_0 = 153.1 km, so conflating the two would assign the wrong frequency to a band, and therefore the wrong group speed. For each band in Figure 3 we take h_{ref} to be the median bathymetric depth beneath the digitized wavefront, and report the resulting period in Table 1.

2.5 Backprojection

2.5.1 Formulation

Each band-passed wavefront (e.g. Figure 3) is received by the backprojection code, which we call *tsbp*, as an ordered polyline of N points $\mathbf{x}_j$, j = 1,2, ... N, digitized along a single crest. Because SWOT images each pixel at a distinct instant along its orbit, every point carries an observation time t_j, measured in minutes after the earthquake origin time and taken from the acquisition time of the nearest SWOT pixel. These are real per-pixel acquisition times rather than interpolated values, and they are what convert a purely geometric constraint into a constraint on both location and time.

We ask, of each wavefront independently and without reference to any source model, where and when it was emitted. Let S denote a candidate emission point on a regular grid spanning the source region and the intervening ocean, $T_j(S)$ is the tsunami travel time between S and $\mathbf{x}_j$, and τ the emission time as minutes after earthquake origin time. If the front was radiated from a single point at a single instant and has propagated freely since, then

$$t_j = \tau + T_j(S) \quad \text{for all j.} \tag{8}$$

The back-projection maps how well each candidate source S satisfies Equation (8), for the wave of the appropriate frequency, over the true bathymetry.

Table 1. *Wave parameters of the three dispersion bands from Figure 3. For each band, n is the number of digitized fronts and h_{ref} is the median bathymetric depth beneath them, at which the dispersion relation $\omega^2 = gk\cdot\tanh(kh_{ref})$, with $k = 2\pi/\lambda$ and $g = 9.8$ m s^{-2}, is evaluated for the band's in-situ central wavelength λ. Listed are the angular frequency ω, period T, group speed c_g, the shallow-water speed $\sqrt{(gh_{ref})}$, their ratio, and the deep-water wavelength $\lambda_0 = \lambda / \tanh(kh_{ref})$. Dispersion strengthens as the band shortens ($c_g / \sqrt{(gh)}$ falls from 0.82 to 0.65), and the deep-water wavelength exceeds the in-situ wavelength throughout, since all three bands lie in the intermediate-depth regime ($kh_{ref} \approx 0.66, 0.81, 1.06$).*

Band (km)	n	h_{ref} (m)	λ (km)	ω (rad s^{-1})	T (s)	c_g (ms^{-1})	√(gh) (m s^{-1})	c_g / √(gh)	λ_0 (km)
50–60	9	5782	55	0.02545	247	196.0	238.0	0.82	95
40–50	10	5827	45	0.03031	207	180.8	239.0	0.76	67
30–40	10	5885	35	0.03715	169	157.1	240.2	0.65	45

2.5.2 The candidate source stack

Evaluating Equation (8) requires $T_j(S)$ for every wavefront point and every candidate cell. We obtain it by exploiting the reciprocity of travel time in a fixed slowness field,

$$T(S \rightarrow x_j) = T(x_j \rightarrow S), \tag{9}$$

which allows us to trace rays outward from each SWOT observation point and read the travel time at every candidate emission source, rather than shooting rays from every source toward the observations. This inverts the cost of the calculation such that a dozen to a hundred wavefront points require the same number of ray fans, whereas a candidate grid of the size used here would require several thousand. Reciprocity holds exactly for the ray equations of Section 2.4, since the slowness field is fixed once ω is resolved for the band.

Then, for each $\mathbf{x}_j$ we launch a fan of rays spanning ±60° about the bearing from $\mathbf{x}_j$ to the centroid of the candidate region, at 0.005° azimuthal spacing, and integrate them with the numerical scheme of Section 2.4 at a time step of 10 s for up to 90 min. The ray set is gridded onto a regular 0.2° map that retains the first-arrival time in each bin, gaps between adjacent rays inside the fan cone are filled by linear interpolation from first-arrival seeds, and the resulting continuous field is sampled bilinearly at the centers of the 0.1° candidate grid. Cells beyond the ray hull, in ray shadows, or over land remain undefined.

A candidate emission source is retained only if it is reached by at least 80% of the wavefront points. Cells falling below this coverage threshold are masked. This guards against misfits computed from a small and geometrically biased subset of the front, which occurs at the periphery of the fan and in shadow zones behind steep bathymetry.

2.5.3 The emission time search

Because τ, the emission time, is unknown with a bounded lower limit by the origin time, we can scan for it. Define a misfit function for each emission source and emission time pair

$$\mathrm{R}(\mathrm{S},\tau) = \sqrt{\frac{1}{N}\sum_j\left(\tau + \mathrm{T}_j(\mathrm{S}) - \mathrm{t}_j\right)^2}\ , \ \tau \geq 0. \qquad (10)$$

Minimizing R over the candidate geographic grid and over a discrete grid of emission times returns a joint estimate (S*, τ*) of where the crest began to propagate freely and when. Since $T_j(S)$ is already stacked, the scan requires no further ray tracing. We sweep τ from 0 to 60 minutes in steps of 1 minute.

Two summaries of Equation (10) are reported. The first is the misfit map at the best emission time, R(S, τ*), which shows where the crest could have originated. The second, and the more informative, is the profile

$$P(\tau) = min_{S\in\mathcal{S}} R(S,\tau), \qquad (11)$$

which shows how well the crest can be explained as a function of emission time alone, having optimized the location at each τ. P(τ) is the quantity that determines whether an emission delay is resolved, and we report it for every band.

Finally, we note that every band-passed wavefront (Figure 3) is back-projected independently, with its own resolved wave, its own stack, and its own search. We deliberately form no joint misfit across bands. Combining them would presuppose a common emission point and time, which is precisely the proposition under test in this work. The independent solutions are collated for comparison, and no result in this paper averages or otherwise combines them.

2.5.4 Evaluating the reliability of recovered source locations

The emission-time search returns a best-fitting location and emission time for each wavefront, but a single crest constrains these only to the extent that its shape and timing distinguish one candidate from another. As shown in Sections 3.1 and 3.2, the constraint is strongly anisotropic: displacing a candidate along the propagation direction (the ray that connects the emission source to the observation point) raises every travel time by nearly the same amount, which the free emission time absorbs. Thus, emission time trade off along that direction and are jointly far better resolved across it than along it. As a result of this a single best-fit point therefore misrepresents the result; we resolve this by quantifying the resolution of each front by a bootstrap that propagates the two ways a digitized crest is uncertain.

The first is the precision with which an individual point is placed on a visible crest of the wavefront, which we treat as an independent displacement normal to the crest with standard deviation (σ_n). The second, and the larger, is a coherent error in the crest, since a hand-digitized front may be collectively shifted or rotated relative to the true wavefront; we represent this as a rigid translation and rotation of the entire polyline with standard deviations (σ_{shift}, σ_{rot}). Independent per-point noise alone would average out over the N points and badly understate the true uncertainty, so the coherent term is essential and in practice dominates. The values of each uncertainty used in the bootstrap are in Table 2.

For each front we generate N_b = 200 realizations of the digitized crest under these perturbations and repeat the full emission-time search on each. This yields a cloud of location and emission time solutions that carries both the picking error we injected and the intrinsic along-propagation degeneracy, since each realization slides to its own best point along that direction. We summarize the location cloud by its empirical 68% region, drawn on maps as a confidence ellipse whose elongation records the degeneracy directly, and we report the emission time as the 16th, 50th, and 84th percentiles of the cloud rather than a symmetric interval, because the $\tau \geq 0$ bound makes the distribution asymmetric for the earliest, promptly radiated fronts.

Table 2. *Uncertainties used in bootstrap analysis for each wavelength band from Figure 3*

Band (km)	σ_n (km)	σ_{shift} (km)	σ_{rot} (°)
50–60	9	5782	55
40–50	10	5827	45
30–40	10	5885	35

3. Results and Discussion

3.1 Validating the approach, backprojection of the main arrival

We first back-project the leading front, which we label α_0, digitized from the unfiltered swath (Figure 6a), it provides a test against an independently known source. α_0 is the long-wavelength arrival radiated promptly from the coseismic deformation, and its location and origin time are constrained by seismic, geodetic, and DART observations (Ruiz-Angulo et al., 2025; Shibata et al., 2025; Sepúlveda et al., 2026). Its wavelength (Figure 3b) places it close to the shallow-water limit, where the group speed lies within ~1% of $\sqrt{(gh)}$ (Figure 4), so we process it with the non-dispersive speed. Recovering the known source from α_0 alone, using no source model, tests the ray geometry, the per-pixel timing, and the misfit construction against a known answer, independently of the dispersive treatment used for the trailing fronts.

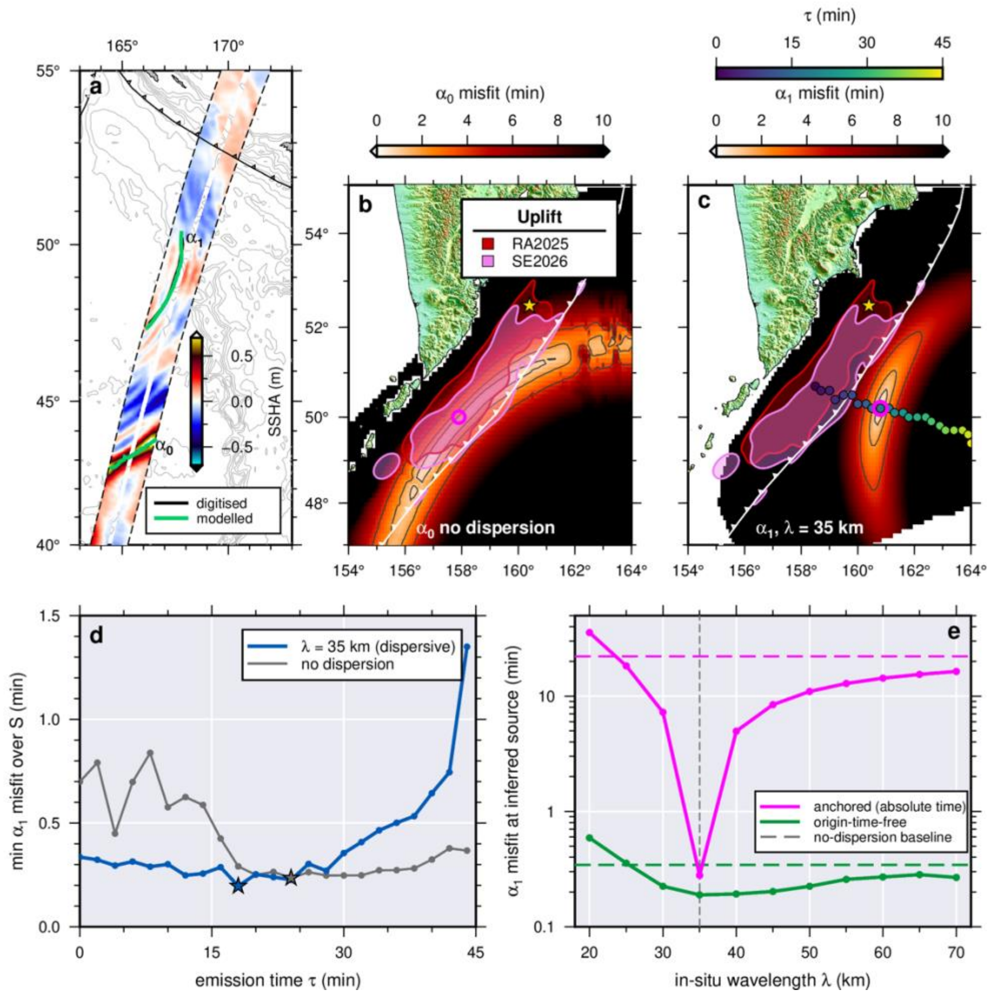

Figure 6. *SWOT wavefront back-projection. (a) Sea-surface-height anomaly (SSHA) across the SWOT swath with the two digitized wavefronts (black; leading α_0, trailing α_1) and their best-fit modelled fronts (green). (b) Misfit over candidate source locations, S, for α_0 (no dispersion) and, (c) for α_1 (dispersive, in-situ wavelength λ = 35 km); gold star, epicenter; magenta circle, best source; white barbed line, trench; shaded polygons, coseismic uplift models (RA2025, SE2026). In (c), dots trace the best source colored by emission time τ. (d) Minimum misfit over S versus τ for α_1: dispersive (λ = 35 km, blue) and non-dispersive (grey), minima starred. (e) Misfit at the inferred α_1 source versus assumed λ for the anchored (absolute-time, magenta) and origin-time-free (green) metrics; dashed lines mark the no-dispersion values, the vertical line λ = 35 km. Both minimize at λ ≈ 35 km.*

Figure 6a shows α_0 digitized on the SWOT SSHA field, together with the front traced forward from its best-fit source. The α_0 misfit map (Figure 6b) has a low-misfit valley of <0.2 min misfit that overlaps the source region defined by both prior uplift models (Ruiz-Angulo et al., 2025; Sepúlveda et al., 2026). The forward-modelled crest for the best-fit source (green, Figure 6a) reproduces the digitized front. The method therefore locates the leading arrival at the known source without any prior on where that source lies.

The valley in the misfit is arc-shaped, tracing the set of candidate sources that lie at nearly equal distance from the digitized front; these all reproduce the observed arrival times about equally well. That the candidates sources, lying at a range of distances from the front, each paired with a compensating emission time, explain the crest almost equally well is expected (Section 2.5.4). The validation criterion is accordingly that the arc pass through the known source, which it does.

Two points of significance follow. First, the 0.2 min floor recovered here can be treated as an empirical resolution of the method on the real bathymetry, with real crest-picking error, for a front of this length and quality. It is the reference against which every trailing front is read: a later front that cannot be explained below this floor is potentially being propagated with the wrong physics, and one that reaches it is fit as well as the leading arrival. Second, the success of the non-dispersive back-projection for α_0 confirms the components that are common to every front, so that when a trailing front requires the dispersive speed to be fit (Section 3.2), the difference can be attributed to the wave model rather than to the geometry, the timing, or the misfit.

3.2 Analysis of dispersed waves

Behind the leading front, the SWOT swath records a train of shorter-wavelength waves whose origin is the subject of this section and the next. We first establish that the train is dispersive and resolve its wavelength content (Figure 2), map where each wavelength band sits within the swath (Figure 3), quantify the wave-speed differences those wavelengths imply (Figure 4,5), and demonstrate that the back-projection recovers the physical wavelength of a trailing front (Figure 6). Localization of the trailing fronts follows in Section 3.3.

The multitaper spectra of Figure 2 provide the wavenumber-domain evidence. The profile crossing the leading front is dominated by wavelengths near and above 60 km, while profiles taken progressively further into the trailing train carry increasing power at shorter wavelengths and develop distinct spectral peaks below 60 km (Figure 2b). As noted, this progression, longer components leading and shorter components trailing, is the defining signature of frequency dispersion. The spectra also establish that the short-wavelength energy is coherent and organized rather than noise, and that it is resolvable down to roughly 30 km, which sets the bands we isolate for back-projection..

Band-pass filtering the swath (Figure 3) shows that the dispersed waves of different wavelengths occupy different parts of the wavefield. The somewhat longer 60–70 km and 50–60 km bands (Figure 3c, d) contain coherent waves confined to the region immediately behind the leading front, with little or no signal north of about 47°N. Meanwhile the shorter 40–50 km and 30–40 km bands (Figure 3e, f) extend much further north, reaching at least the latitude at which the swath crosses the Emperor Seamount chain and probably beyond it. The ordering itself, shorter bands lagging further behind the leading front, is what dispersion predicts (Figure 4,5) and its presence in the imagery is independent confirmation of the phenomena.

Whether that ordering fully accounts for the spatial pattern of the localized wavefronts is less clear, and is the question Section 3.3 is designed to answer. Two end-member interpretations bound it. If the trailing waves are the source-radiated dispersive tail, their extent along the swath is governed by group speed alone and should vary smoothly with wavelength. The 50–70 km bands, confined close behind the leading front, are consistent with this picture. The concentration of the shortest bands at and beyond the Emperor Seamounts is more suggestive. One would expect that deformation from large coseismic source, would be relatively "smooth" at short wavelengths and thus would radiate limited energy in the 30–50 km band. In this view, simple group-speed lag would not preferentially deposit that energy at a major bathymetric obstacle the wavefield must cross. We note that the shortest bands extend furthest north, toward the source side of the swath, which is the direction in which slower, more strongly dispersed waves lag at a fixed observation time. Group-speed lag alone can thus potentially account for some of the spatial ordering. But, whether the northward extent of the 30-50 km bands is fully explained or requires short-wavelength energy generated near the source (Ruiz-Angulo et al., 2025) and carried outward, cannot be settled from the imagery; we return to it in Section 3.3, where each band is back-projected to its apparent origin.

The wave-speed differences these wavelengths imply are large, which is what makes the choice of wave physics consequential. Figure 4 shows the group speed, the speed at which wave energy and therefore travel time propagate, as a function of local wavelength and depth. At the representative source-to-swath depth of 5,500 m, the group speed of the observed bands falls well below the shallow-water value c_{sw}: it is 89% of c_{sw} at 70 km, 81% at 50 km, and 62% at 30 km. Over the roughly 600 km separating the source region from the swath, adopting the shallow-water speed underestimates the travel time by about 5 min at 70 km, 10 min at 50 km, and nearly 27 min at 30 km. Figure 4 also shows that the discrepancy grows with depth at fixed wavelength, and that the 30–70 km band sits on the steep part of the curve at abyssal depths, where the sensitivity to wavelength is greatest.

Figure 5 shows the potential effect on back projection, here we trace two ray fans from a point source near the Kamchatka centroid, one under shallow-water physics and one for a 30 km dispersive wave, over the true bathymetry. The dispersive rays are slower everywhere, by roughly 40% across the abyssal plain. They also follow markedly different paths, because a dispersive wave refracts according to its phase speed rather than the depth-controlled shallow-water speed (Section 2.4). The two fans diverge most where they cross the trench and the seamount province, the regions of strongest bathymetric gradient. Back-projecting a dispersed front under shallow-water physics therefore assigns it both the wrong travel times and the wrong ray geometry, and the recovered origin moves accordingly. This is why the shallow-water treatment, which locates the leading arrival successfully (Section 3.1), is fundamentally inappropriate for the trailing fronts.

Figure 6 demonstrates these points on the data. Where the leading front was located with shallow-water physics (Section 3.1), a trailing front cannot be. Figure 6c back-projects an example wavefront we label as α_1, using the dispersive group speed; its low-misfit valley locates seaward of the trench. The shallow-water treatment does not fit it at any comparable level because the shallow water wave travels so fast that the code attempts to locate the source in the Sea of Okhotsk behind the Kuril Islands and outside our allowed domain. The recovery of a physical wavelength is made explicit in Figure 6e, where we fixes the source at the inferred α_1 location and sweep the assumed wavelength from 20 to 70 km. Both misfit quantities plotted there are limiting cases of the emission-time misfit of Equation (10). The origin-time-free misfit takes the emission time as fully free, minimizing R over τ at each candidate, so it measures only the agreement of the wavefront's shape; the anchored misfit instead fixes the emission time and so retains the absolute arrival times. We use both here solely to test wavelength recovery; all trailing-front locations in this paper come from the emission-time search. What's important is that the Figure shows that both misfit metrics form two-sided bowls minimizing at $\lambda \approx 35$ km, coincident with an analysis of the 30–40 km band-pass that follows in Section 3.3. The anchored misfit spans about two decades across the sweep and is the sharper constraint, because it does not let the emission time absorb a timing error; the origin-time-free misfit is gentler, reaching 0.19 min at 35 km against 0.34 min under shallow-water physics. The method therefore measures the correct in-situ wavelength of a dispersed front, which validates the dispersive wave model that the leading arrival could not test.

One feature of the approach has a direct bearing on Section 3.3. The emission-time search on its own is somewhat insensitive to dispersion (Figure 6d). Dispersion slows the modelled travel times of α_1 by a near-uniform 8 min, from a mean of about 45 to 53 min, and because a free emission time absorbs any uniform offset, the best-fitting emission time moves earlier, from 26 to 18 min, compensating the slower propagation while leaving the reconstructed absolute arrival unchanged. The minimum misfit as a function of emission time is consequently almost identical for the dispersive and non-dispersive wave models. It is the absolute-time view, or fixing the source independently, that exposes the wavelength (Figure 6e); the emission-time search locates and orders the fronts but does not by itself constrain the wave model. The emission times we report for the trailing fronts in Section 3.3 are therefore computed with each band's validated in-situ wavelength, and their interpretation must account for the distance–emission-time trade-off inherent to a single front (Section 2.5.4).

3.3 Location of the dispersed wave sources

Having established that the trailing fronts require the dispersive treatment (Section 3.2), we back-project each band-passed wavefront with the emission-time search (Section 2.5.3) and quantify the resolution of each solution with the calibrated bootstrap of Section 2.5.4. The result is Figure 7, which shows, for all twenty-eight trailing fronts across the three bands, the 68% source region of each front on the map together with the distribution of recovered emission times.

Before reading individual fronts, one expectation follows from the physics alone. The trailing waves travel at their slow dispersive group speed (Figure 4), so a short-wavelength front imaged roughly 600 km from the source region some 70 minutes after the earthquake cannot in general have been radiated from the coseismic source at the origin time and still arrive where and when SWOT observes it. Reconciling the observed position with the observed time requires, for at least some fronts, an orig in displaced from the coseismic source, an emission delayed after the origin time, or both. The back-projection is the tool that determines which, front by front, rather than assuming any of them.

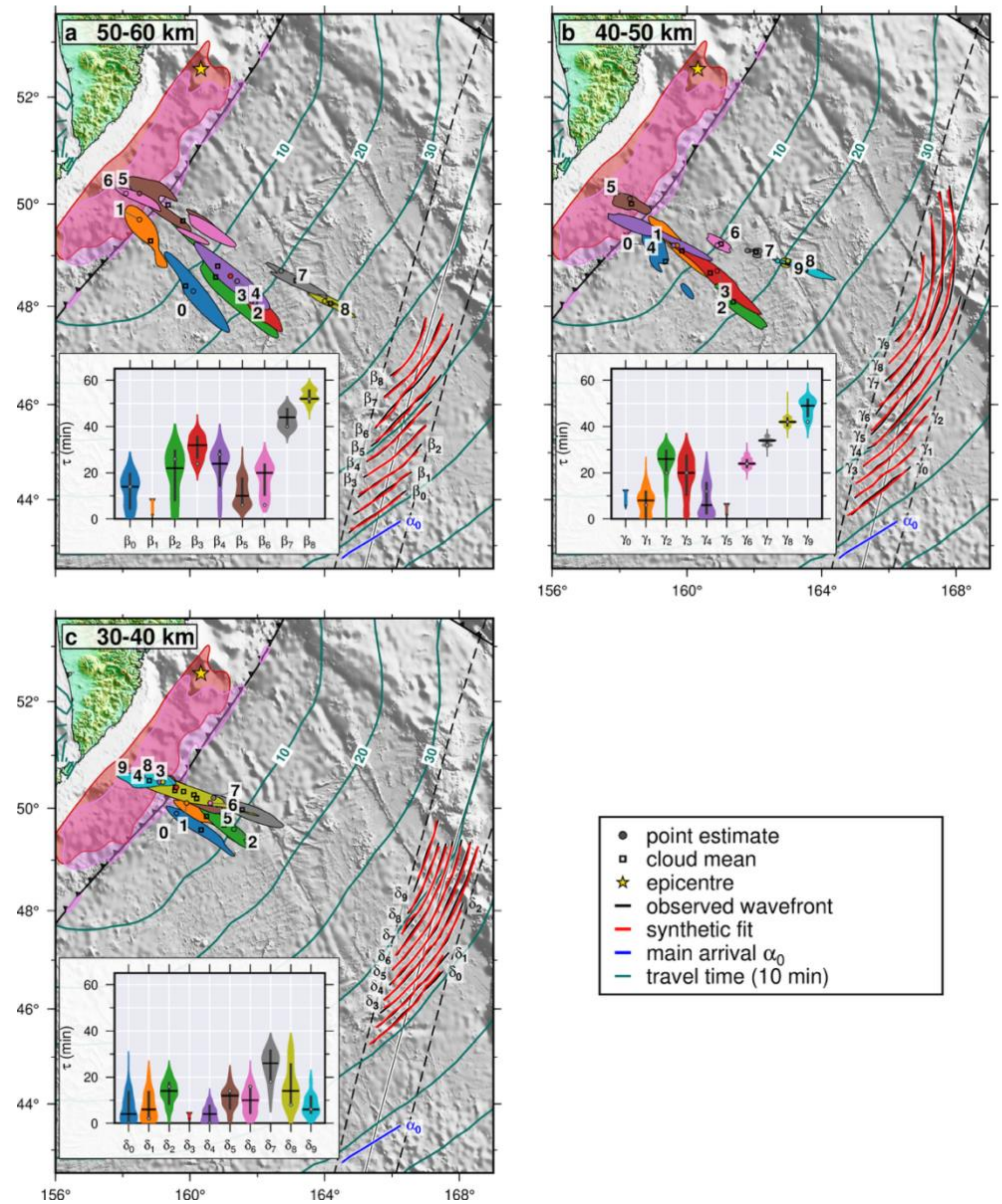

***Figure 7**. Bootstrap source-cloud reconstructions for the three dispersion bands: (a) 50–60 km (β), (b) 40–50 km (γ), (c) 30–40 km (δ). Filled polygons are the empirical 68% source regions for each back-projected wavefront, colored and numbered by front index; the dot marks the point estimate, the open square the bootstrap mean, and the yellow star the epicenter. In the SWOT swath, digitized crests (black) are shown with their emission-time best fits (red), plus the α_0 main arrival (blue). Teal contours are modelled tsunami travel time (10-min interval, labelled along 51°N) for a shallow water wave originating from the Kamchatka source region as in Figure 1. Insets give the emission time τ of each wavefront (violins of the raw bootstrap replicates; bar = 16–84th percentile, line = median, diamond = point estimate, downward arrow = prompt/upper-bound), on a common τ axis across all bands.*

3.3.1 Resolution varies strongly between fronts

The bootstrap makes plain that the fronts are not equally well constrained (Figure 7). For a single crest the set of candidate origins and the emission-times from the grid search trade position along the ray connecting source to observation (Section 2.5.4). For many fronts the 68% confidence region is a long, thin lobe elongated along that ray, tens to a few hundred kilometers in extent, and for these the location and the emission time are individually poorly determined. Front β_2 is a good example (Figure 7a) with the long axis of the confidence region spanning ~200km and the possible emission times being in the range 0-40 min. Other fronts, generally the longer or more strongly curved crests, yield compact regions and tightly determined emission times such as fronts γ_8 and γ_9 (Figure 7b). therefore, we cannot treat every front as a measurement with equal trustworthiness. This is not to say that the front and its sources are not a real present phenomena in SWOT. Instead this means that we cannot interpret it confidently given the scatter in the back projection results. Thus, in what follows we distinguish the fronts that are resolved, whose bootstrap regions are compact and whose emission-time intervals are narrow, from those that are not. Of the twenty-eight fronts (Figure 7), 10 are robustly resolved in both position and emission time; the remainder are elongated along the arc, ambiguous in emission time, or both.

3.3.2 Consistency checks

The recovered locations and emission times are not independent, and their relationship provides an internal consistency check. A front whose origin is far from the coseismic source must, because the dispersed waves are slow, have a late emission time; meanwhile a far origin combined with emission time soon after the coseimsic source (a prompt emission) is close to physically impossible, since such a wave could not have covered the distance in the available time. All fronts respect this. Those that back-project far from the source region are also late, and those that are prompt sit near the source; no front falls in the forbidden far-and-prompt combination. The loci and the emission times are therefore mutually consistent rather than independently noisy, which supports the coherence of the solutions.

3.3.3 Findings by wavelength band

In this regard, the clearest results come from the 40-50 km wavelength band (Figure 7b). The emission times are ordered along the train: the earliest fronts are prompt or near-prompt, and the median emission time rises monotonically through the later fronts, reaching 49 mins for the last one. The late fronts of this band, γ_6-γ_9, yield compact bootstrap regions that sit well outside the source region, close to the SWOT swath, at emission times of ~20-50 mins. These are the best-resolved dispersed sources in the dataset, and they are simultaneously displaced from the coseismic region and substantially delayed.

The 50-60 km band (Figure 7a) resolves at its tail but not in its middle. The two latest fronts, β_7 and β_8, are compact and late, at roughly 45 and 51 minutes, and lie outside the source region, echoing the late 40-50 km fronts. The earlier and middle fronts of this band, by contrast, have broad regions elongated along the arc and emission-time distributions that span much of the range, and we do not localize them save for β_1 whose confidence region sits partially withint he coseismic source zone and has emission times < 7 mins. Nonetheless, in general, for this band the emission-time ordering is present but noisier than in the 40-50 km band.

The 30-40 km band (Figure 7c) is the least resolved of the three, though at least we can say it lacks wave sources emitted late and far from the coseismic source. This is a direct consequence of its larger picking uncertainty (Section 2.5.4). Most of its fronts have broad bootstrap regions, and only its tail approaches the resolution seen in the other bands. Emission times are low through much of the band with wide intervals. We therefore draw on this band mainly for its consistency with the other two at the resolved end, rather than as an independent constraint.

Across all three bands, the resolved late fronts share a common character: their bootstrap regions lie outside the source region defined by the two prior tsunami source models (Ruiz-Angulo et al., 2025; Sepulveda et al., 2026; Figure 7), they are displaced toward the SWOT swath, and their emission times are delayed by tens of minutes relative to the origin time. The resolved prompt fronts, where present, sit within or adjacent to that source region. We turn next to Section 3.4 to address the question of what physical processes these two populations can represent.

3.4 Mechanisms of the displaced, delayed sources

The back-projection places a subset of the trailing fronts clearly outside the coseismic source region and at emission times well after the origin time (Section 3.3). Here we ask what the recovered locations and emission times might imply about how these waves were produced. We first establish, without recourse to the back-projection, that the trailing train as a whole arrives too late to have all been radiated dispersively from the source region, then we use the recovered sources to characterize the delay, and finally weigh candidate mechanisms.

3.4.1 The trailing train arrives later than a source-region origin allows

A statement about the trailing waves can be made from the observations alone, independently of any back-projection. For each front we know the time SWOT imaged it (~69.5-71.5 mins for all fronts), and we can compute, over the true bathymetry, the travel time from the coseismic source region to the front's observed position for both a shallow-water wave and a dispersive wave of the appropriate wavelength (Figure 8). These define the earliest and latest arrival times (green shaded region) consistent with a source-region origin: nothing can outrun the shallow-water wave, and a dispersive wave of the observed wavelength is the slowest a directly radiated front could be. Figure 8 shows that in all three bands, the majority of the wavefronts arrive later than the dispersive travel time from the source region. Most of the wavetrain after the main tsunami arrival therefore arrives too late to be explained as short-wavelength energy radiated from the coseismic source and dispersed in transit, the direct-dispersion delay characterized for far-field tsunamis by Glimsdal et al. (2013), Okal and Synolakis (2016), and Poupardin et al. (2018). Because this simple calculation uses only observed arrival times and forward travel times, it does not depend on the ray-tracing back-projection or its uncertainties, beyond a far-field loading delay omitted from the forward travel times that Section 3.5 shows is too small at this range to affect the result.

3.4.2 The recovered sources are displaced and progressively delayed

The back-projection resolves where and when this late energy originated. Ten fronts are robustly classified as originating outside the source region and late (Section 3.3; Figure 9), they are stable

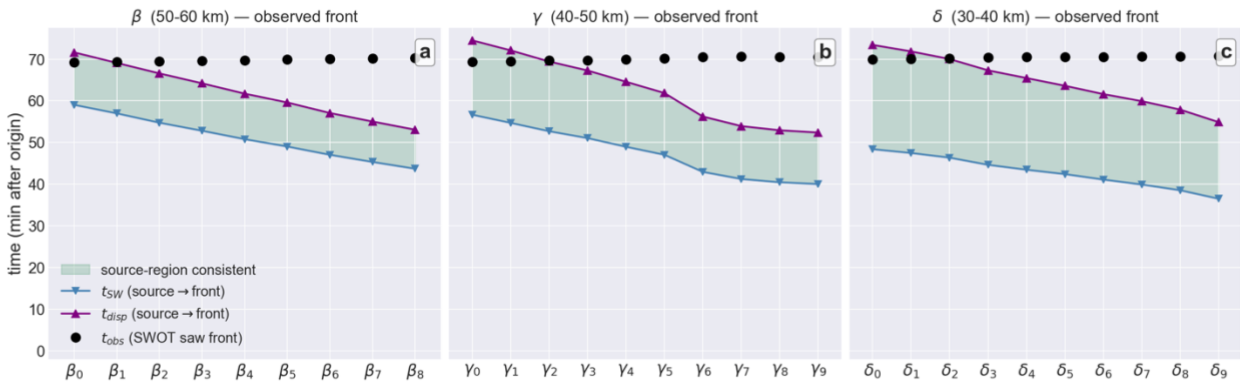

***Figure 8**. Observed-front admissibility.(a-c) For each wavelength band (β 50–60 km, γ 40–50 km, δ 30–40 km; panels a–c), the time at which SWOT imaged each digitised front, t_{obs} (black, the mean of the back-projection's per-pixel SWOT times), compared with the shallow-water (t_{SW}, blue) and dispersive (t_{disp}, purple) travel times from the coseismic source region to that front's mean position. The green band (t_{SW}, t_{disp}) marks arrivals consistent with a source-region origin; t_{obs} above it is later than a dispersive wave, below t_{SW} is faster than shallow water. Fronts are ordered by index within each band.*

across all sensitivity settings. Their recovered locations and emission times are given in Table 3. Two features organize them.

First, the emission time increases with distance from the source. Ordering the ten fronts by the shallow-water travel time from the source to their recovered locations, a proxy for distance, the recovered emission time rises almost monotonically with it (rank correlation 0.90). The nearest displaced sources were emitted around 24 to 26 minutes after the origin, the farthest around 49 to 52 minutes.

Second, and more diagnostically, the delay is not incurred all at once. For each front we compare its emission time to the shallow-water arrival time of the fast-leading shallow-wave at that same location, the earliest moment any energy from the earthquake could have reached it (Figure 10). Every displaced front was emitted well after this floor, by 12 to 25 minutes, and this excess delay grows with distance from the source (Table 3; rank correlation 0.64). A wave produced by a single event, for instance a one-time scattering of the leading shallow water wave off a fixed bathymetric feature such as the Avachinsky transform, would show a roughly constant delay past the arrival of this incident wave. The observed delay instead accumulates along the path. This points to energy that is progressively retarded as it propagates outward, rather than generated at a single place and time.

We verified that this delay is not an artifact of the wavelength assumed in the dispersive travel time. Recomputing the dispersive arrival at the short-wavelength edge of each band (Figure 10), the slowest admissible wave, still leaves every front as originating later than what a directly radiated dispersive wave would allow (Table 3, final column positive throughout), with the single exception of γ2, whose margin is small. The displaced, delayed character of these sources is therefore robust to

Table 3. *Recovered sources of the ten fronts robustly classified as originating outside the source region and late (Outside Late; Section 3.3), ordered by shallow-water travel time from the source, a proxy for distance. Columns give the bootstrap cloud-mean location; the emission time τ as 16th, 50th, and 84th percentiles of the bootstrap distribution (minutes after origin); the shallow-water travel time t_{SW} from the coseismic source to the recovered location; and the delay of the median emission time past the earliest possible arrival of energy at that location ($\tau_{50} - t_{SW}$) and past a directly radiated dispersive wave ($\tau_{50} - t_{disp}$). All times in minutes. Emission time increases with distance from the source (rank correlation 0.90) and the delay past t_{SW} grows with distance (rank correlation 0.64), indicating delay that accumulates along the propagation path rather than incurred at a single location.*

Front	Lon (°E)	Lat (°N)	τ_{16}	τ_{50}	τ_{84}	t_{SW}	$\tau_{50} - t_{SW}$	$\tau_{50} - t_{disp}$
δ7	161.55	49.97	18	26	32	9.7	16.3	11.5
γ6	161.02	49.23	22	24	26	10.5	13.5	10.1
β4	160.82	48.80	14	24	30	12.0	12.0	9.4
γ7	162.05	49.07	32	34	34	15.8	18.2	13.3
γ2	161.38	48.09	20	26	30	18.2	7.8	2.0
β3	161.93	48.07	26	32	36	20.1	11.9	7.6
γ8	162.99	48.87	40	42	44	20.8	21.2	14.8
β7	163.15	48.51	40	44	48	22.8	21.2	16.4
γ9	163.53	48.73	44	49	52	23.7	25.3	18.1
β8	164.17	48.06	50	52	56	29.2	22.8	16.6

the within-band spread of wavelengths.

3.4.3 Potential Mechanisms

The progressive accumulation of delay with distance constrains the candidate mechanisms we consider to three.

A first possibility is that the short-wavelength waves are radiated directly from short-scale coseismic deformation near the trench and simply disperse during transit, the interpretation favored by Sepúlveda et al. (2026) and, for the 2009 Samoa and 2011 Tohoku tsunamis, by Saito et al. (2011, 2014) and Zhou et al. (2012). This is excluded for the dispersed fronts by Figures 8,9 and by the computations in Figure 10, they either arrive later than any dispersive wave from the source region could have originated or are emitted with a significant delay after origin time. Their energy did not travel a direct dispersive path from the coseismic source to the swath imaged by SWOT.

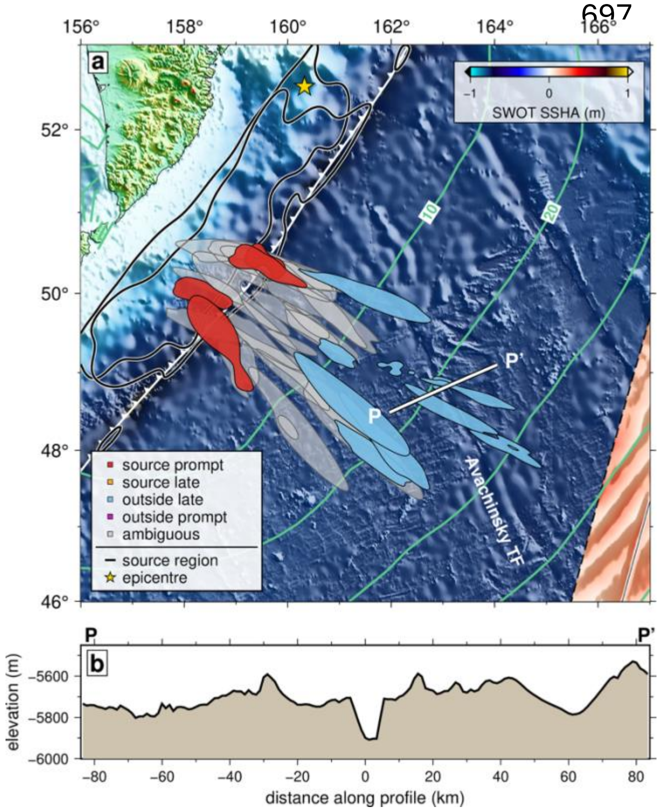

***Figure 9**. Bootstrap source-cloud reconstructions classified by category. (a) 68% source regions colored by category, source prompt (red), outside late (blue), ambiguous (grey); cource late or outside prompt (purple) the tsunami source regions from Ruiz-Angulo et al. (2025) and Sepulveda et al. (2026) are shown. Tsunami travel-time isochrones are for the shallow-water propagations speed (10-min, green), and the epicenter is the yellow star. The white line P–P' marks the bathymetry transect across the Avachinsky Transform Fault. (b) Bathymetry along P–P', showing the ~250 m fault valley at profile center.*

A second possibility is generation at a single bathymetric feature, such as scattering of the leading wave where it crosses the Avachinsky transform, which the SWOT swath intersects (Figure 9a). It is a significant feature with significant bathymetry differences across it and a relevant wavelength (Figure 9b). However, we find that this is not well supported. Only three of the ten dispersed fronts lie within a few tens of kilometers of the transform, and even those were emitted roughly 20 minutes after the leading wave reached it, rather than promptly as a single scatter would require. The remaining fronts lie 45 to 145 km from the feature. No single fixed source reproduces both the spread of locations and the distance-dependent delay.

The interpretation most consistent with the observations is that the trailing energy is progressively delayed through distributed interaction with the rough abyssal seafloor along the propagation corridor. The northwest Pacific seafloor traversed by these waves carries pervasive abyssal-hill fabric, seamounts, and fracture zones and transforms (Figure 9a), and a wavefield crossing such terrain is scattered, refracted, and partially retarded continuously rather than at any one location. Under this interpretation, the apparent emission time recovered by the back-projection is the time at which coherent short-wavelength energy began to propagate freely toward the swath from a given point along the corridor, and its increase with distance reflects the accumulation of delay over a longer interaction path. This is the en-route generation anticipated qualitatively by Ruiz-Angulo et al. (2025), here localized and timed. In that work they also anticipated that resonance mechanisms in the near-shore environment such as edge waves and shelf resonance could also radiate late, short wavelength dispersive energy, we do not find evidence for this as none of our located fronts originate within the coseismic source region with a significant delay.

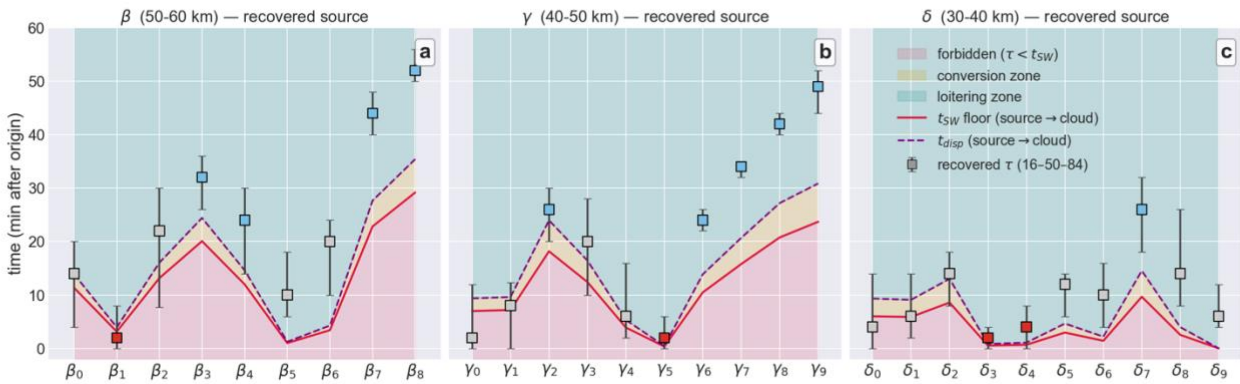

Figure 10. *Recovered-source admissibility. For the same bands and fronts (a–c), the recovered emission time τ (squares: median with 16th–84th-percentile bootstrap bars), evaluated at each front's recovered cloud-mean location and colored by its geometric–temporal category (see Figure 9). Background zones are set by the travel times from the source region to that location: $\tau < t_{SW}$ (red) is forbidden, this is earlier than the coseismic wave can arrive; $[t_{SW}, t_{disp}]$ (gold) is the conversion zone; $\tau \sim t_{disp}$ (dashed purple) is originated as dispersive; $\tau > t_{disp}$ (teal) is loitering. Every front's τ84 lies at or above its t_{SW} floor, so all recovered emission times are physically admissible.*

We do not claim to identify the specific physical process that is responsible for each wavefront however. Distributed scattering off abyssal-hill topography, mode conversion, interaction with the fracture-zone system, and partial trapping and re-radiation all predict energy that is delayed and displaced, and the back-projection, which recovers where and when a front began to propagate freely but not how it was generated, cannot distinguish among them. Doing so would require forward hydrodynamic modeling of the wavefield over the real bathymetry, which is beyond the scope of this study. What the observations establish is narrower and, we argue, robust: a substantial part of the short-wavelength tail imaged by SWOT did not originate at the coseismic source, but was emitted from points along the propagation path, progressively later with distance, consistent with cumulative interaction between the tsunami and the seafloor it crossed.

3.5 Limitations of our approach and unanswered questions

The dominant limitation in our approach is resolution. A single wavefront constrains its source to an arc of candidate origins at nearly equal distance, and the emission-time search trades position along that arc against emission time (Section 2.5.4). For many fronts this degeneracy is significant: their bootstrap regions are elongated tens to a few hundred kilometers along the source to observation ray and neither location nor emission time is individually determined. Of the twenty-nine trailing fronts, fewer than half are robustly classified, and the results rest on that resolved subset. The unresolved fronts are reported as such and carry no interpretation. Resolution is poorest for the shortest-wavelength band, whose faint, closely spaced crests are the hardest to digitize and therefore carry the largest picking uncertainty.

The source uncertainty we report propagates digitization error, estimated by blind re-picking of every front, through the back-projection. It does not include error in the bathymetry, in the removal of the large-scale oceanographic background from the SWOT field, or in the assumption that each digitized crest is a single coherent wavefront rather than an interference pattern. The last of these is the most consequential and the least quantified: a curve that is not a coherent propagating front can still back-project to an apparent origin, and we guard against this only by retaining crests that are visually continuous across the swath.

The method recovers where and when a front began to propagate freely, not how it was generated. The apparent emission point of a wave produced during propagation need not coincide with a physical source, and ray theory, which can refract an existing wave but cannot scatter or diffract one, does not model the generation process at all. Our inference that the displaced fronts are produced by distributed interaction with the seafloor (Section 3.4) is therefore constrained by the recovered locations and times but is not a forward demonstration of any specific mechanism. Distinguishing among scattering, mode conversion, and trapping would require forward hydrodynamic modeling over the real bathymetry.

Finally, the dispersive travel times use a single representative wavelength per band. The observed fronts span a range of wavelengths within each band, and although we have shown the principal results to be robust to this spread (Section 3.4), a fully consistent treatment would carry each front's own wavelength through the calculation.

Our travel times also omit the delay that elastic loading, seawater compressibility, and gravitational potential change impart on far-field tsunamis (Tsai et al., 2013; Watada et al., 2014; Baba et al., 2017), an effect that grows with distance and reaches 10 to 15 minutes at trans-Pacific range. Over the roughly 600 km to the swath it is of order a minute, well below the 12 to 25 minute delays in Table 3 and too smooth across the recovered sources to produce their distance-dependent trend, with the marginal front γ_2 the one case where it is an appreciable fraction of the excess.

None of these limitations overturns the central result, which is deliberately narrow: a resolved subset of the short-wavelength fronts imaged by SWOT originated away from the coseismic source and progressively later with distance. The open questions concern the physical mechanism of that delayed generation and the fate of the many fronts the method cannot yet localize.

3.6 Other uses of this approach and future work

The approach developed here is not specific to this event. It requires a two-dimensional image of a tsunami wavefield in which coherent fronts can be digitized and time-tagged, and back-projected over known bathymetry. As SWOT continues to operate and its swath intermittently intersects future tsunamis, each such capture becomes a candidate for the same analysis. This underscores a broader point about the observation itself: the wide-swath geometry resolves wavefront curvature, propagation direction, and the two-dimensional arrangement of a dispersive train, none of which a nadir altimeter recovers from its single along-track profile. The information that makes back-projection possible, the shape and orientation of a front rather than its amplitude alone, is precisely what swath altimetry adds over conventional nadir measurements.

The same principle extends to an observing system with complementary strengths. Distributed acoustic sensing (DAS) on seafloor telecommunications cables measures strain along a single line (e.g. Tonegawa & Araki, 2024), so it does not image a wavefield in two dimensions the way SWOT does. It does, however, resolve the passage of a tsunami in time along that line at high sampling, which SWOT, imaging each location once, does not. A DAS cable therefore yields a time-distance record, and coherent wavefronts appear as moveout in a Hovmoller (time versus along-cable distance) representation (e.g. Melgar & Ruiz-Angulo, 2018). Fronts traced in that domain carry an absolute arrival time at every point along the cable, which is the same ingredient the emission-time search exploits here, and they could be back-projected in the same way. Where SWOT trades time resolution for a two-dimensional snapshot, DAS trades the second spatial dimension for continuous time, and either provides the time-tagged fronts the method needs.

This may prove useful beyond retrospective source characterization. Tsunamis are still occasionally observed with no immediately clear seismic or obvious geophysical source (Mizutani & Melgar, 2023; Sandanbata et al., 2024), and the growth of seafloor DAS along existing cable routes will increase the chance that such an event is recorded in time-distance detail near its origin. Back-projection of the observed fronts, requiring no prior source model, offers a way to locate and time the origin of a wavefield directly from its own geometry, which is exactly the situation in which a source is otherwise hard to establish.

4. Conclusions

We back-projected the dispersive tsunami wavefield imaged by SWOT following the 2025 M8.8 Kamchatka earthquake, tracing individual band-passed wavefronts to a source location and an emission time with a dispersive ray-tracing engine and no assumed source model. The method recovered the known source region from the leading front, and per-front resolution was quantified by a bootstrap calibrated against blind re-digitization. Because a single front constrains an arc of source positions traded against emission time, many fronts were not localizable and were left uninterpreted. Ten trailing fronts were robustly localized outside the coseismic source region and at emission times well after the origin, stable across the analysis. Their emission time increased with distance from the source, and each was emitted later than the earliest possible arrival of energy from the earthquake at its location, by a margin that grew with distance. The trailing train as a whole was shown, independently of the back-projection, to arrive too late to have been radiated dispersively from the source region. We concluded that a substantial part of the short-wavelength tail imaged by SWOT was generated during propagation, progressively delayed through cumulative interaction with the seafloor, rather than radiated from the coseismic source. We did not resolve the specific process responsible, which would require forward hydrodynamic modeling over the real bathymetry. The approach requires only a time-tagged image of coherent wavefronts over known bathymetry, and applies to future wide-swath altimetry captures and, in the time-distance domain, to distributed acoustic sensing on seafloor cables.

Acknowledgments

We thank Ignacio Sepulveda for fruitful discussions on tsunami science. This research was supported by the Cascadia Region Earthquake Science Center (CRESCENT), funded via National Science Foundation Cooperative Agreement EAR-2225286, and additional funding from the United States Geological Survey Cooperative Agreement #G25AC00531 and Pacific Gas and Electric Company. DM is also partially supported by NASA grant #80NSSC23K1326 and NSF-MGG grant #2325310

Open Research

All data and modeling codes used are open source. Surface water and ocean topography (SWOT) altimetry data were available at https://www.aviso.altimetry.fr/en/data/products/sea-surface-height-products/global/swot-l3-ocean-products.html . Shuttle Radar Topography Mission (SRTM) 15+ bathymetry data were available at https://portal.opentopography.org/raster?opentopoID=OTSRTM.122019.4326.1 . The tsunami ray tracing in this study was performed with TsunamiTrace, an open-source Python package for tsunami ray tracing on a sphere. Version 1.0 is archived on Zenodo (Melgar, 2026a), and the actively developed repository is available at https://github.com/dmelgarm/TsunamiTrace/. The source back-projection was carried out with tsbp, an open-source package that builds on TsunamiTrace; version 1.0 it is archived similarly on Zenodo (Melgar, 2026b), and its live repository is available at https://github.com/dmelgarm/tsunamiBP/. Both packages are released under the GNU General Public License v3 and include documentation and worked examples. All websites were last accessed in July 2026.

References

Baba, T., Allgeyer, S., Hossen, J., Cummins, P. R., Tsushima, H., Imai, K., ... & Kato, T. (2017). Accurate numerical simulation of the far-field tsunami caused by the 2011 Tohoku earthquake, including the effects of Boussinesq dispersion, seawater density stratification, elastic loading, and gravitational potential change. *Ocean Modelling*, *111*, 46-54.

Glimsdal, S., Pedersen, G. K., Harbitz, C. B., & Løvholt, F. (2013). Dispersion of tsunamis: does it really matter? *Natural Hazards and Earth System Sciences*, *13*(6), 1507-1526.

Gusman, A. R., Murotani, S., Satake, K., Heidarzadeh, M., Gunawan, E., Watada, S., & Schurr, B. (2015). Fault slip distribution of the 2014 Iquique, Chile, earthquake estimated from ocean-wide tsunami waveforms and GPS data. *Geophysical Research Letters*, *42*(4), 1053-1060.

Gusman, A. R. (2026). Re-estimation of the 1952 Kamchatka earthquake source using tsunami data and calibration from the 2025 tsunami event. Earth, Planets and Space, 78(1), 107.

Hayashi, Y. (2008). Extracting the 2004 Indian Ocean tsunami signals from sea surface height data observed by satellite altimetry. *Journal of Geophysical Research: Oceans*, *113*(C1).

Hill, E. M., Borrero, J. C., Huang, Z., Qiu, Q., Banerjee, P., Natawidjaja, D. H., ... & Sieh, K. (2012). The 2010 Mw 7.8 Mentawai earthquake: Very shallow source of a rare tsunami earthquake determined from tsunami field survey and near-field GPS data. *Journal of Geophysical Research: Solid Earth*, *117*(B6).

Kajiura, K. (1963). The leading wave of a tsunami. *Bulletin of the Earthquake Research Institute*, *41*, 535-571.

Kirby, J. T., Shi, F., Tehranirad, B., Harris, J. C., & Grilli, S. T. (2013). Dispersive tsunami waves in the ocean: Model equations and sensitivity to dispersion and Coriolis effects. *Ocean Modelling*, *62*, 39-55.

Kiser, E., & Ishii, M. (2017). Back-projection imaging of earthquakes. *Annual Review of Earth and Planetary Sciences*, *45*, 271-299.

Kulikov, E. (2006). Dispersion of the Sumatra tsunami waves in the Indian Ocean detected by satellite altimetry. *Russian Journal of Earth Sciences*, *8*(4), ES4004.

MacInnes, B. T., Weiss, R., Bourgeois, J., & Pinegina, T. K. (2010). Slip distribution of the 1952 Kamchatka great earthquake based on near-field tsunami deposits and historical records. *Bulletin of the Seismological Society of America*, *100*(4), 1695-1709.

Melgar, D., Fan, W., Riquelme, S., Geng, J., Liang, C., Fuentes, M., ... & Fielding, E. J. (2016). Slip segmentation and slow rupture to the trench during the 2015, Mw8. 3 Illapel, Chile earthquake. *Geophysical Research Letters*, *43*(3), 961-966.

Melgar, D., & Ruiz-Angulo, A. (2018). Long-lived tsunami edge waves and shelf resonance from the M8. 2 Tehuantepec earthquake. *Geophysical Research Letters*, *45*(22), 12-414.

Melgar, D. (2026a). dmelgarm/TsunamiTrace: TsunamiTrace v1.0.0 (Version v1.0.0) [Computer software]. Zenodo. https://doi.org/10.5281/zenodo.21477863

Melgar, D. (2026b). dmelgarm/tsunamiBP: tsbp v1.0.0 (Version v1.0.0) [Computer software]. Zenodo. https://doi.org/10.5281/zenodo.21477874

Mizutani, A., & Melgar, D. (2023). Potential volcanic origin of the 2023 short-period tsunami in the Izu Islands, Japan. *Seismica*, *2*(2).

Morrow, R., Fu, L. L., Ardhuin, F., Benkiran, M., Chapron, B., Cosme, E., ... & Zaron, E. D. (2019). Global observations of fine-scale ocean surface topography with the surface water and ocean topography (SWOT) mission. *Frontiers in Marine Science*, *6*, 232.

Okal, E. A., Piatanesi, A., & Heinrich, P. (1999). Tsunami detection by satellite altimetry. *Journal of Geophysical Research: Solid Earth*, *104*(B1), 599-615.

Okal, E. A., & Synolakis, C. E. (2016). Sequencing of tsunami waves: why the first wave is not always the largest. *Geophysical Journal International*, *204*(2), 719-735.

Pinegina, T. K., Ozerov, A. Y., Tsvetkov, V. A., Kotenko, T. A., Mironov, I. K., Bourgeois, J., ... & Lukashenko, D. R. (2025). Tsunami from the Mw 8.8 Kamchatka Earthquake of 29 July 2025 on the East Coast of Kamchatka and the North Kuril Islands: TK Pinegina et al. *Pure and Applied Geophysics*, 1-25.

Poupardin, A., Heinrich, P., Hébert, H., Schindelé, F., Jamelot, A., Reymond, D., & Sugioka, H. (2018). Traveltime delay relative to the maximum energy of the wave train for dispersive tsunamis propagating across the Pacific Ocean: the case of 2010 and 2015 Chilean Tsunamis. *Geophysical Journal International*, *214*(3), 1538-1555.

Prieto, G. A. (2022). The multitaper spectrum analysis package in Python. *Seismological Society of America*, *93*(3), 1922-1929.

Romano, F., Piatanesi, A., Lorito, S., D'agostino, N., Hirata, K., Atzori, S., ... & Cocco, M. (2012). Clues from joint inversion of tsunami and geodetic data of the 2011 Tohoku-oki earthquake. *Scientific reports*, *2*(1), 385.

Ruiz-Angulo, A., Melgar, D., De Marez, C., Deniau, A., Nencioli, F., & Hjörleifsdóttir, V. (2025). SWOT Satellite Altimetry Observations and Source Model for the Tsunami from the 2025 M 8.8 Kamchatka Earthquake. *The Seismic Record*, *5*(4), 341-351.

Sandanbata, O., Satake, K., Takemura, S., Watada, S., Maeda, T., & Kubota, T. (2024). Enigmatic tsunami waves amplified by repetitive source events near Sofugan volcano, Japan. *Geophysical Research Letters*, *51*(2), e2023GL106949.

Satake, K. (1994). Mechanism of the 1992 Nicaragua tsunami earthquake. *geophysical research letters*, *21*(23), 2519-2522.

Satake, K., Fujii, Y., Harada, T., & Namegaya, Y. (2013). Time and space distribution of coseismic slip of the 2011 Tohoku earthquake as inferred from tsunami waveform data. *Bulletin of the seismological society of America*, *103*(2B), 1473-1492.

Saito, T., Satake, K., & Furumura, T. (2010). Tsunami waveform inversion including dispersive waves: The 2004 earthquake off Kii Peninsula, Japan. *Journal of Geophysical Research: Solid Earth*, *115*(B6), B06303.

Saito, T., Ito, Y., Inazu, D., & Hino, R. (2011). Tsunami source of the 2011 Tohoku-Oki earthquake, Japan: Inversion analysis based on dispersive tsunami simulations. *Geophysical Research Letters*, *38*, L00G19.

Saito, T., Inazu, D., Miyoshi, T., & Hino, R. (2014). Dispersion and nonlinear effects in the 2011 Tohoku-Oki earthquake tsunami. *Journal of Geophysical Research: Oceans*, *119*(8), 5160-5180.

Sepúlveda, I., Nilsson, B., Yu, Y., Carvajal, M., Brandin, M., Gabriel, A. A., & Sandwell, D. (2026). SWOT detects dispersive tsunami tied to a near-trench source in the 2025 Kamchatka earthquake. *Science*, *391*(6792), 1368-1372.

Shibata, R., Kubo, H., & Suzuki, W. (2025). Source process of the 2025 Mw 8.8 Kamchatka Peninsula, Russia, earthquake revealed by back-projection and waveform inversion. *Authorea Preprints*.

Song, Y. T., Fukumori, I., Shum, C. K., & Yi, Y. (2012). Merging tsunamis of the 2011 Tohoku-Oki earthquake detected over the open ocean. *Geophysical Research Letters*, *39*(5).

Tanioka, Y., Nishimura, Y., Hirakawa, K., Imamura, F., Abe, I., Abe, Y., ... & Masaka, S. (2004). Tsunami run-up heights of the 2003 Tokachi-oki earthquake. *Earth, planets and space*, *56*(3), 359-365.

Tappin, D. R., Grilli, S. T., Harris, J. C., Geller, R. J., Masterlark, T., Kirby, J. T., ... & Mai, P. M. (2014). Did a submarine landslide contribute to the 2011 Tohoku tsunami? *Marine Geology*, *357*, 344-361.

Thomson, D. J. (1982). Spectrum estimation and harmonic analysis. *Proceedings of the IEEE*, *70*(9), 1055-1096.

Tsai, V. C., Ampuero, J. P., Kanamori, H., & Stevenson, D. J. (2013). Estimating the effect of Earth elasticity and variable water density on tsunami speeds. *Geophysical Research Letters*, *40*(3), 492-496.

Tonegawa, T., & Araki, E. (2024). High-frequency tsunamis excited near Torishima Island, Japan, observed by distributed acoustic sensing. *Geophysical Research Letters*, *51*(11), e2024GL108714.

Vinogradova, N. T., Pavelsky, T. M., Farrar, J. T., Hossain, F., & Fu, L. L. (2025). A new look at Earth's water and energy with SWOT. *Nature Water*, *3*(1), 27-37.

Watada, S., Kusumoto, S., & Satake, K. (2014). Traveltime delay and initial phase reversal of distant tsunamis coupled with the self-gravitating elastic Earth. *Journal of Geophysical Research: Solid Earth*, *119*(5), 4287-4310.

Ye, L., Bai, Y., Si, D., Lay, T., Cheung, K. F., & Kanamori, H. (2022). Rupture model for the 29 July 2021 MW 8.2 Chignik, Alaska earthquake constrained by seismic, geodetic, and tsunami observations. *Journal of Geophysical Research: Solid Earth*, *127*(7), e2021JB023676.

Yue, H., Lay, T., Rivera, L., An, C., Vigny, C., Tong, X., & Báez Soto, J. C. (2014). Localized fault slip to the trench in the 2010 Maule, Chile Mw= 8.8 earthquake from joint inversion of high-rate GPS, teleseismic body waves, InSAR, campaign GPS, and tsunami observations. *Journal of Geophysical Research: Solid Earth*, *119*(10), 7786-7804.

Zhou, H., Wei, Y., & Titov, V. V. (2012). Dispersive modeling of the 2009 Samoa tsunami. *Geophysical Research Letters*, *39*(16), L16603.